Microstructure evolution and very-high-cycle fatigue crack initiation behavior of a structural steel with two loading intermittence modes

Yadong Zhou, Jingyu Sun, Xiangnan Pan, Guian Qian [*], Youshi Hong [*]

State Key Laboratory of Nonlinear Mechanics, Institute of Mechanics, Chinese Academy of Sciences, Beijing 100190, China
School of Engineering Science, University of Chinese Academy of Sciences, Beijing 100049, China

ARTICLE INFO

ABSTRACT

The effects of fatigue loading intermittence on specimens manufactured on two locations in a railway wheel were experimentally investigated: (i) in the rim and (ii) web plate (WP). The specimens with 50 ms pause presented a substantially lower fatigue strength in comparison to those with 300 ms pause. The microstructure evolution indicated the occurrence of martensitic transformation and discontinuous dynamic recrystallization. Rim and WP show respective preference for crack initiation, i.e. inclusion or matrix. Slip on {1 1 0} and {1 1 2} plane families prevails in ferrite. The pearlitic lamellae aligned at 45° relative to applied tension indicates that crack initiates and propagates along the ferrite-cementite interface due to stress concentration as a result of inhomogeneous deformation.

1. Introduction

Repair and replacement of high-speed rail wheels, due to fatigue damage, already have been a significant proportion of operation costs [1,2]. Between maintenance cycles, the wheels are inevitably subjected to over 10^5 cyclic fatigue loading. Therefore, high-cycle fatigue (HCF, i. e., fatigue failure between 10^5 and 10^7 cycles) and very-high-cycle fatigue (VHCF, i.e., fatigue failure beyond 10^7 cycles) behaviors of wheels and crack initiation mechanism have been proved crucial for cost reduction [3,4]. Even though wheel steels with distinct microstructures, such as advanced bainitic steel [5,6], bainite-martensite multiphase steel [7], spheroidized pearlitic steel [8] have been widely developed, the traditional lamellar pearlitic steel is still widely used in high-speed rail wheels because of its excellent wear and fatigue performance [9,10]. Hence, a systematic experimental investigation on the pearlitic steel should be conducted to illuminate the mechanism responsible for VHCF failure.

On the other hand, ultrasonic fatigue testing is an efficient way to conduct VHCF test. Thanks to the extremely high loading frequency of 20 kHz, ultrasonic fatigue test remarkably reduces the testing time. More importantly, it is argued that the frequency effect can be ignored in some cases of low stress amplitudes [11–13]. However, self-heating induced in ultrasonic fatigue test, especially in those with smaller loading intermittence. Intermittence may have a significant effect on the

fatigue behavior [14]. From the perspective of wheel, high temperature of 700 °C exists in actual working condition due to wheel-rail rolling and sliding [15]. Therefore, in this study a strategy of fatigue loading with smaller intermittence was adopted to simulate this condition [14–16].

It has been ascertained that the mechanical property of pearlitic steel is associated with pearlite interlamellar spacing, and the relationship between tensile property and interlamellar spacing has been reported [17–19]. However, effects of interlamellar spacing on fatigue behavior still remain unclear. Therefore, samples manufactured on two locations (rim and web plate) [20] of a railway wheel with different interlamellar spacing were obtained to explore this effect. On the other hand, microstructure evolution is also important to understand because of its substantial effect on fatigue behavior. For instance, the so-called white etching layer is a typical microstructure layer induced in rolling contact fatigue (RCF), which is brittle and susceptible to crack formation [21,22]. Liu et al. [23] proposed that cracks are mainly propagated at the interface between the grain refinement zone and the unrefined zone during RCF process. Previous investigations mainly focus on the microstructure evolution in RCF, and the change of microstructure in ultrasonic fatigue for pearlitic steel has not yet been fully studied.

The crack initiation mechanism of high-strength steels has been explored [24–26], and two typical crack initiation types have been defined by Zhao et al. [7], namely "non-inclusion induced crack initiation" (NIICI) and "inclusion induced crack initiation"(IICI). However,
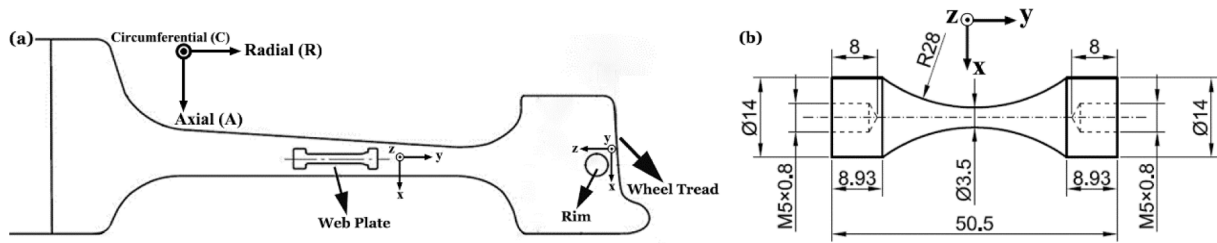

Fig. 1. (a) Test specimen sampling locations and (b) specimen dimensions (units: mm).

Table 1
Chemical composition of experimental steel (weight, %).

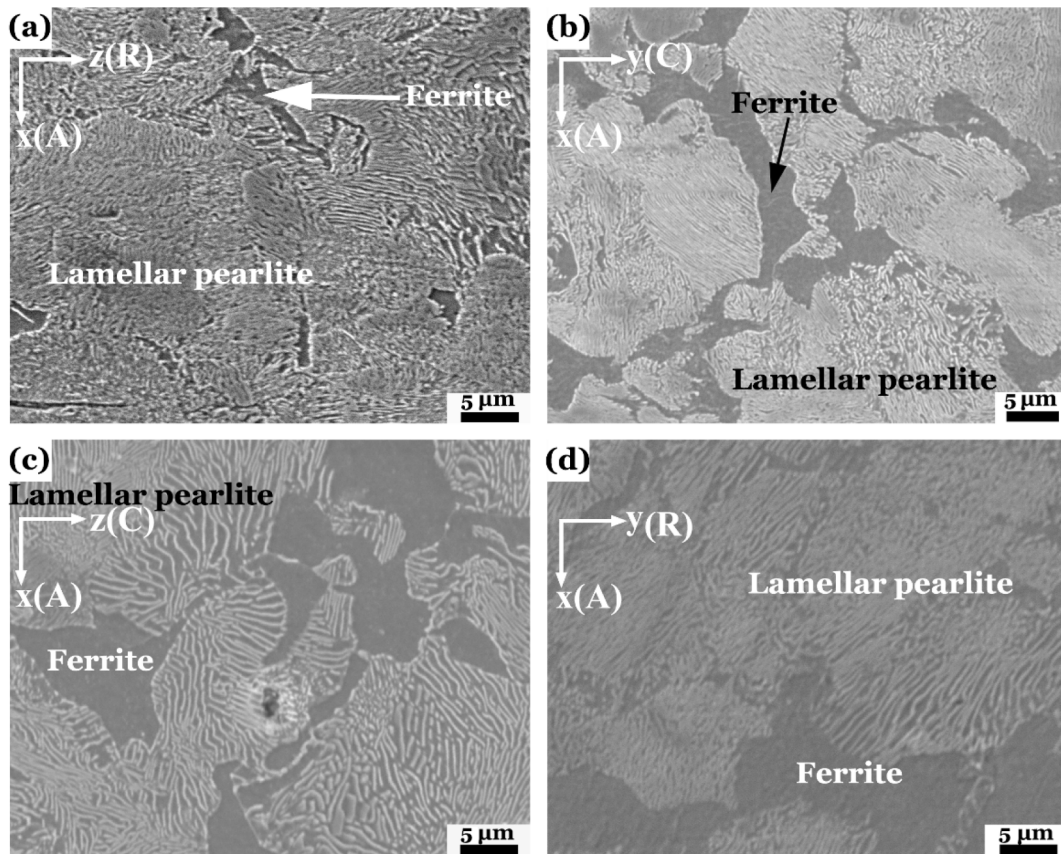| Fe	C	Si	Mn	P	S	Cr	Cu	Ni	Mo	V
Bal.	0.54	0.30	0.75	0.013	0.007	0.18	0.20	0.10	0.04	0.003

Fig. 2. Microstructure characterization of specimen prior to fatigue test: (a) rim-transverse section (x-z), (b) rim-longitudinal section (x-y), (c) WP-transverse section (x-z), and (d) WP-longitudinal section (x-y).

the investigation into NIICI of pearlitic steel, especially the detailed mechanism, is limited. So far, NIICI phenomenon has only been observed in high strength steels [27–36] and titanium alloys [37,38] in both HCF and VHCF regimes. Based on these observations, several researchers have suggested different mechanisms to explain how facets were formed. Chai et al. [27] proposed that the facet formation was caused by local plastic deformation of soft phase (such as ferrite and austenite). Zhang et al. [28] found that microstructure dominated the failure when the inclusion size was smaller than 1 μm. Pan et al. [37] conclude that crack initiates from large lamellar microstructure domains with certain crystallographic orientation. However, few investigations were conducted connecting spatial orientation of facet with certain slip

systems of grains, and the mechanism of facet formation for pearlitic steel still remains unclear.

In this study, ultrasonic fatigue tests of pearlitic steel extracted from railway wheels were carried out under loading with 50 ms and 300 ms pause. The experimental samples were manufactured from two locations of a railway wheel, namely rim and web plate, aiming to explore different crack initiation mechanisms due to their distinct microstructures. The microstructure evolution due to self-heating induced in the fatigue loading with 50 ms pause was also characterized. In particular, much emphases were put on the mechanism of facet formation since it is rarely investigated compared to the widely observed inclusion induced crack initiation.
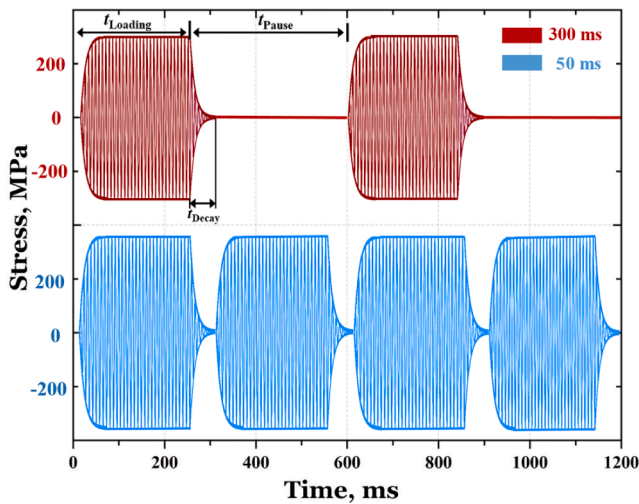
Fig. 3. Schematic diagram of two loading strategies with stress ratio of -1 in ultrasonic fatigue test. 50 ms: loading with 50 ms pause; 300 ms: loading with 300 ms pause; t_{Decay}: duration of loading decreases to zero after excitation electric signal is stopped.

2. Material and experimental procedure

2.1. Material and specimens

The material used in this study, a medium-carbon steel, was cut from an actual high-speed railway train wheel. The specific sampling locations and sampling directions are shown in Fig. 1a. A coordinate system (axial, circumferential, radial direction) was defined for the wheel, and other coordinate systems (x-y-z) were also defined for rim and WP (abbreviation for web plate) respectively. After the machining, the surfaces of all specimens were polished with No.600–2000 abrasive papers and the specimen geometry is shown in Fig. 1b. The chemical composition of the material is listed in Table 1. As shown in Fig. 1a, rim and WP are located in different depths from wheel tread, which experienced different cooling rates during water spray quenching for wheel tread, eventually resulting in different mechanical properties.

The microstructures of rim and WP are presented in Fig. 2, which is ferrite-pearlite microstructure apparently (i.e., proeutectoid ferrite and lamellar pearlite). Pearlitic colonies comprise alternating ferrites and
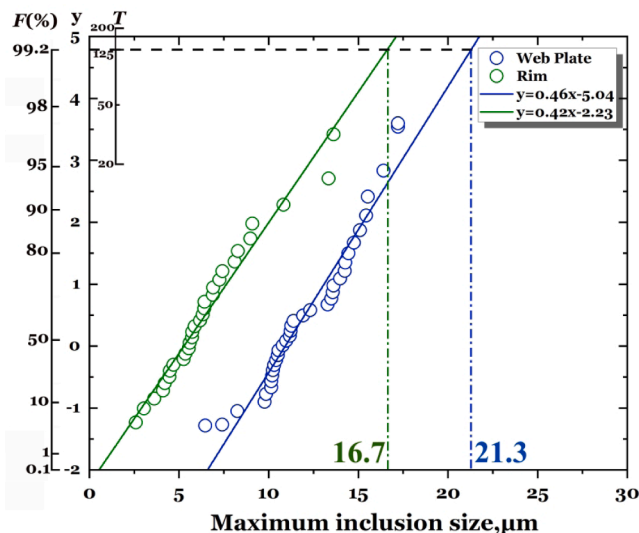

Fig. 4. Gumbel distribution of inclusion size for the specimen machined in the rim and web plate of a railway wheel.

cementite plates, notably, the average pearlitic interlamellar spacing (S_p) of rim is obviously smaller than that of web plate as shown in Fig. 2. The perpendicular line method [39] was used to measure S_p, and the results show that S_p values of rim and WP are 338 ± 34 nm and 432 ± 39 nm ($\pm$means standard deviation separately based on ten measured values), respectively. It is worth noting that the fraction of ferrite in rim is lower than that in WP owing to different cooling rates [20], averagely $22\% \pm 0.9\%$ for rim and $31\% \pm 2.4\%$ for WP ($\pm$ means uncertainty corresponding to 95% confidence).

2.2. Tensile and fatigue test procedure

The mechanical property of materials was tested by a quasi-static tension test (strain rate 10^{-4} s^{-1}) on an MTS 810 system. According to the results, the rim possessed yield strength (with 0.2% plastic strain) of 602 MPa, tensile strength of 930 MPa and uniform elongation of 17%, whereas yield strength, tensile strength and uniform elongation for web plate are 521 MPa, 779 MPa and 21%, respectively. Prior to fatigue test, micro-hardness was measured along transverse and longitudinal sections of specimens with a load of 500 gf (HV$_{0.5}$) and dwell time of 5 s. The results showed a uniform micro-hardness distribution in rim and web plate, averagely 276 HV$_{0.5}$ and 226 HV$_{0.5}$, respectively.

The ultrasonic fatigue test was conducted on a Shimadzu USF-2000 with a frequency of 20 kHz at room temperature and in ambient air with the loading ratio of -1. Two loading intermittence modes were adopted in this investigation including: (a) 300 ms loading with 300 ms pause; (b) 300 ms loading with 50 ms pause. Fig. 3 shows the details of stress variation paths versus time during 300 ms intermittent loading, which contains 300 ms of stable loading, then the excitation electric signal is stopped, followed by a pause of 300 ms (include stress decay time t_{Decay}, about 50 ms, for stress decreasing to zero after excitation electric signal is stopped) [40]. The loading cycles during the attenuation period were not counted in the fatigue life. During fatigue tests of two loading intermittence modes, compressed air was used for gauge section of specimen to cool down through six nozzles. Testo 885 Thermal Imager was used to record temperature variation of specimen's surface.

2.3. Characterization methods of fractography

Fracture surfaces of failed specimens were carefully observed by a scanning electron microscope (SEM, JEOL JSM IT-300). The roughness of fracture surfaces was measured by means of topography analysis using a non-contact optical 3D profilometer (ZYGO Nexview). The profiler uses the scanning white light interferometry (SWLI) technique to examine the microstructure, and the surface topography is of a resolution of 0.1 nm on z (height) direction. The focal plane was defined as $z = 0$.

The scanning area of SWLI was a square box with the size of 1681 μm × 1681 μm, which is large enough to cover the whole rough area (RA) region on a fracture surface. The scanning box was nearly adjusted to the center of an RA region by positioning the specimen. Once scanning was completed, data processing and 3D image reconstruction were then conducted by Matlab software. Thus the topography of every RA region was built in terms of the measured height values (z) marked by different colors.

The micro-hardness along the longitudinal section of different depths from fracture surface was measured by using a Vickers micro-hardness instrument (MVK-H21) with the load of 500 gf (HV$_{0.5}$) for 5 s dwell time. Besides, EBSD (electron backscatter diffraction) samples were taken from failed specimens along the longitudinal section, followed by vibration polishing. EBSD analysis was performed on a Zeiss Gemini 300 SEM equipped with Oxford Symmetry EBSD system with the accelerating voltage of 20 kV, and the specimen tilt-angle of 70°. The step size of the scanning was set as 0.2 μm or 0.03 μm depending on the size of the scanned areas and grains. The thin foils (about 10 μm × 7 μm × 50 nm) were cut by the FIB/SEM dual-beam system (Helios NanoLab G3 CX)
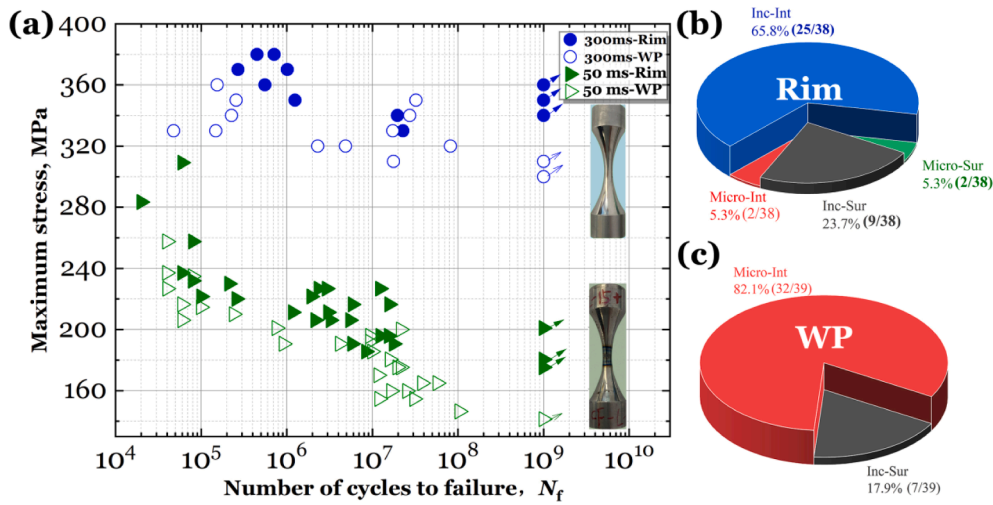
Fig. 5. (a) *S-N* data of specimens subjected to different loading types. 300 ms-Rim: rim specimens of 300 ms pause, 300 ms-WP: web plate specimens of 300 ms pause, 50 ms-Rim: rim specimens of loading with 50 ms pause, 50 ms-WP: web plate specimens of loading with 50 ms pause. The proportion of crack initiation modes in rim (b) and web plate (c). Int: interior. Sur: surface. Mat: matrix. Inc: inclusion.

from inclined facets. Thin foils were characterized by transmission Kikuchi diffraction (TKD, Oxford Symmetry, 30 kV) with specimen tilt-angle of 20° and transmission electron microscopy (TEM, FEI Tecnai G20, 200 kV). Subsequently, the obtained data were post-processed by software AZtecCrystal and GMS 3. The chemical composition analysis of the non-metallic inclusions was conducted by energy-dispersive spectroscopy (EDS) technique on SEM equipped with Oxford-Max^N 50.

3. Results and discussion

3.1. Evaluation of inclusion size

The statistics of extreme values (SEV) [41,42] method was utilized to estimate the maximum inclusion size in a certain area S (units:mm^2). First, a transverse section of the specimen was cut, followed by polishing with No.2000 emery paper. Subsequently, 60 standard inspection areas S_0 with the same size of about 0.077 mm^2 were selected without over-lapping across the cut section. Then, every inclusion of the maximum size $\sqrt{area_{max}}$ within each inspection area was selected and sorted (with $j = 1,...,60$) in ascending order. It is assured that the measured inclusion sizes from 2.59 μm to 17.22 μm can be well described by the Gumbel distribution as shown in Fig. 4. The cumulative distribution function F_j (%), reduced variate y_j and the return period T were readily calculated according to the Eqs. 1–3. Note that the maximum stress appears across the middle section of specimen. Thus the area of circular section (3.5 mm in diameter) was defined as the area of examination S. Therefore, the value of period T can be calculated by Eq. (3) to give about 125 as shown in Fig. 4 by horizontal dashed line. As depicted in Fig. 4, two least square fitting lines showed the linear relationship between the maximum inclusion size $\sqrt{area_{max}}$ and reduced variate y_j. Then, from the intersection points between horizontal dashed line and the fitting lines, two vertical lines were drawn. The estimated maximum inclusion size can be obtained from the corresponding abscissa axis. In this way, the value of $\sqrt{area_{max}}$ for rim is 16.7 μm, which is apparently smaller than that for web plate, i.e. 21.3 μm.

$$F_j = j \times 100/(n+1) \tag{1}$$

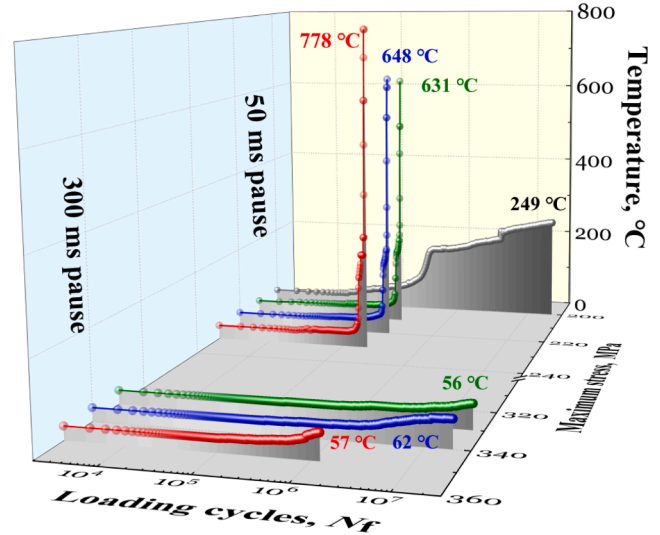$$y_j = -\ln\{-\ln[j/(n+1)]\} \tag{2}$$

$$T = S/S_0 \tag{3}$$

Fig. 6. Surface temperature variation of the gauge section of specimen versus loading cycles with two loading intermittence modes.

3.2. S-N data and temperature variation

Fig. 5a shows the *S-N* data for four groups of specimens obtained from different sites of wheel and subjected to different loading inter-mittence modes. It is clear that the specimens under loading with 50 ms pause presented a substantially poorer performance in comparison to those with 300 ms pause. In addition, rim had superior fatigue proper-ties than web plate. To be more specific, the mean fatigue strength (σ_{w9}, fatigue strength at 10^9 cycles) of 300 ms-Rim, 300 ms-WP, 50 ms-Rim and 50 ms-WP specimens are 350 ± 10 MPa, 305 ± 7 MPa, 185 ± 14 MPa and 141 MPa (± means standard deviation), respectively. It is likely that the decrease in fatigue strength of the specimens with 50 ms pause attributes to self-heating induced in fatigue loading [43,44]. A typical specimen with burnt surface is presented in the lower right corner of Fig. 5.

It is worth noting that for rim specimens (Fig. 5b), fatigue cracks were prone to initiating from CaO·Al$_2$O$_3$ inclusion cluster (89.5%, 34/38), whereas for web plate (WP) specimens (Fig. 5c), fatigue cracks preferred to initiate from matrix (82.1%, 32/39). This difference is due
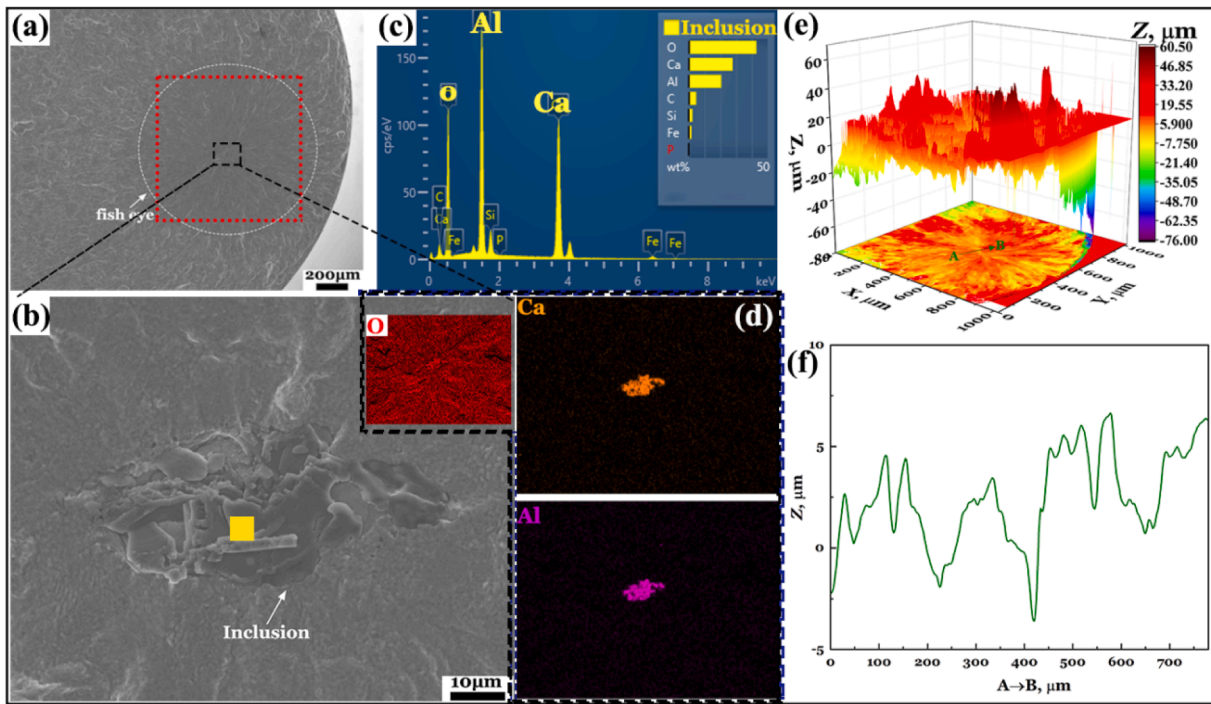
Fig. 7. Fracture surface morphology of rim specimen (rim, $\sigma_{max} = 211$ MPa and $N_f = 3.03 \times 10^6$ cycles, 50 ms pause): (a) SEM image showing crack initiation region of fish-eye; (b) enlarged image of inclusion cluster, yellow square being site of EDS analysis site (c); (d) area-scanning of inclusion cluster; (e) SWLI image of red dotted square in (a) and projection map of height z on the bottom; (f) fracture surface roughness curve along line AB in (e).
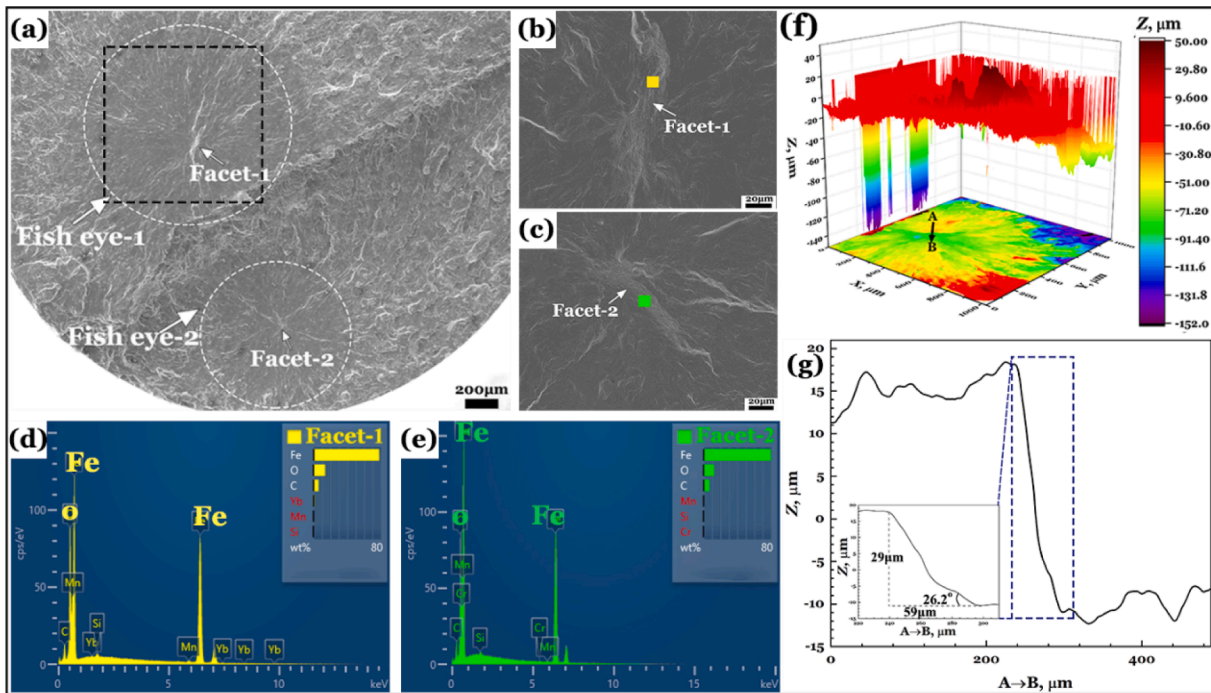

Fig. 8. Fracture surface morphology of web plate (WP, $\sigma_{max} = 160$ MPa and $N_f = 1.66 \times 10^7$ cycles, 50 ms pause): (a) SEM image showing crack initiation region of two fish-eyes; (b) and (c) enlarged images of facet-1 and facet-2 with squares denoting EDS analysis sites (d) and(e); (f) SWLI image of dashed square in (a) and projection map of height z on the bottom; (g) fracture surface roughness curve along line AB in (f) with inset showing inclined angle.

to a larger proportion of ferrite and larger pearlitic interlamellar spacing in WP specimens introduced by smaller degree of undercooling compared with rim specimens, which is attributed to different depths from wheel tread during quenching process. As a result, the inclusion is less critical than matrix for the fatigue failure of WP specimens despite

the fact that relatively larger inclusions existed in WP specimens.

Fig. 6 shows the temperature variation of gauge section of specimens versus loading cycles under different stress amplitudes with two loading intermittence modes. It can be seen that for 50 ms pause mode, temperature increased sharply before it failed and the temperature variation
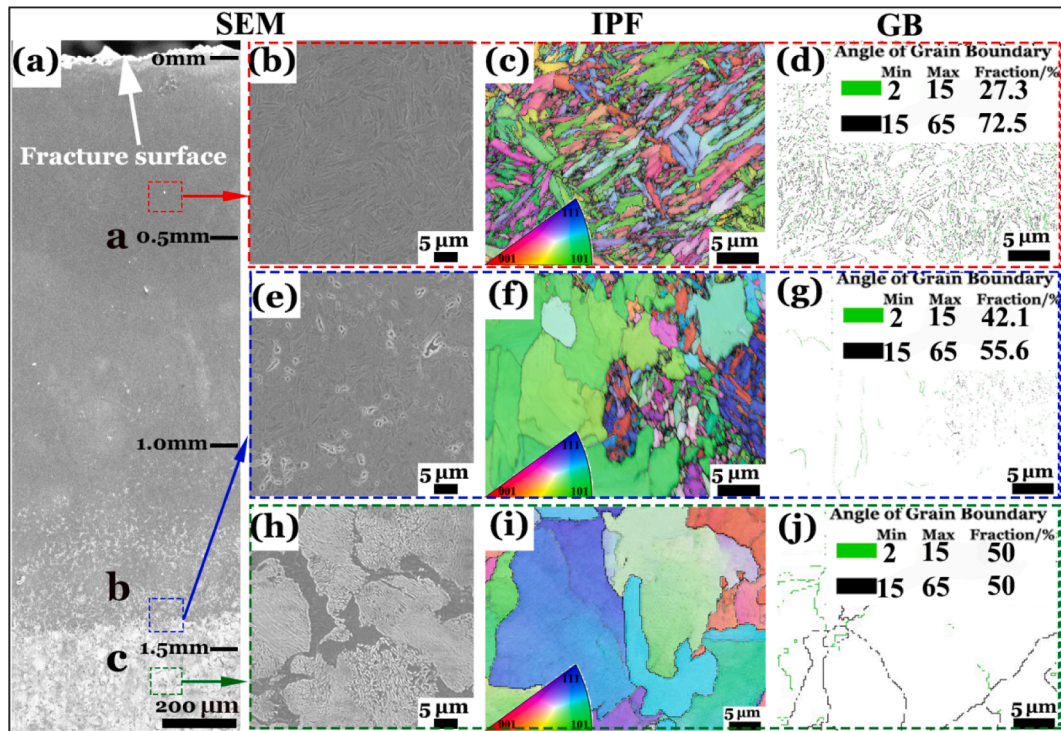
Fig. 9. Microstructure evolution as a function of depth from the fracture surface of a rim specimen with 50 ms pause (σ_{max} = 220 MPa and N_f = 1.01 × 10⁵ cycles): (a) global view; (b–d) severe plastic deformation (SPD) zone taken from upper region; (e–g) transition zone at 1.4 mm below the surface; (h-j) matrix material at 1.7 mm from the surface.

is dependent on stress amplitude, which increases with the rise of stress amplitude. But for specimens with 300 ms pause, the temperature variation is less apparent, with a gradual rise of about 30 °C even for different stress amplitudes.

3.3. Fractography observations

The SEM, SWLI and EDS observations for typical fracture surfaces of rim and web plate are illustrated in Figs. 7 and 8. The SEM observations demonstrated that fish-eye is the typical internal cracking feature for the pearlitic steel in both HCF and VHCF regimes and its diameter is from

hundreds of micrometers to about 1.1 mm. Moreover, SWLI observations depicted fracture surface roughness and obtained inclined angle through drawing a line perpendicular to the extension direction of facet. In addition, EDS analyses of inclusion (rim) and facet (WP) verified the chemical composition.

Fig. 7a is a typical fracture morphology of inclusion induced crack initiation in rim specimens (50 ms pause) and Fig. 7b is an enlargement of black dashed box in Fig. 7a. It is apparent that inclusion cluster is of an elliptical shape and its chemical composition is CaO and Al_2O_3. As shown in Fig. 7e, the roughness within fish-eye ranged from −76 μm to 60.5 μm, and the height value only varied no more than 10 μm (Fig. 7f)
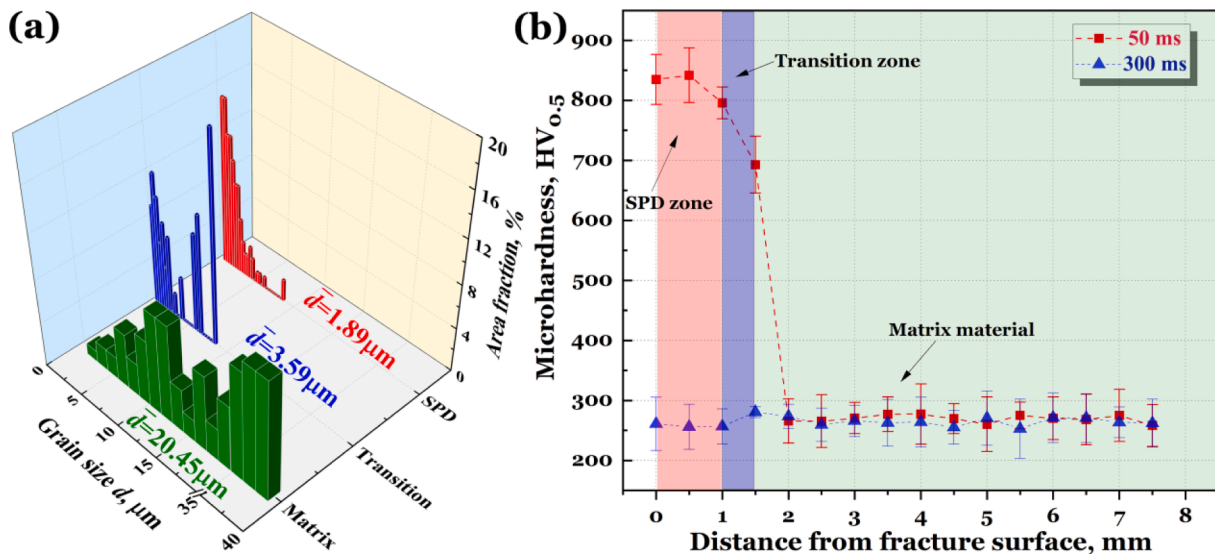

Fig. 10. (a) Grain size statistics of specimen in Fig. 9 and (b) micro-hardness along longitudinal section of specimens (50 ms: σ_{max} = 220 MPa and N_f = 1.01 × 10⁵ cycles; 300 ms: σ_{max} = 330 MPa and N_f = 1.8 × 10⁷ cycles) subjected to fatigue loading with 50 ms and 300 ms pause.
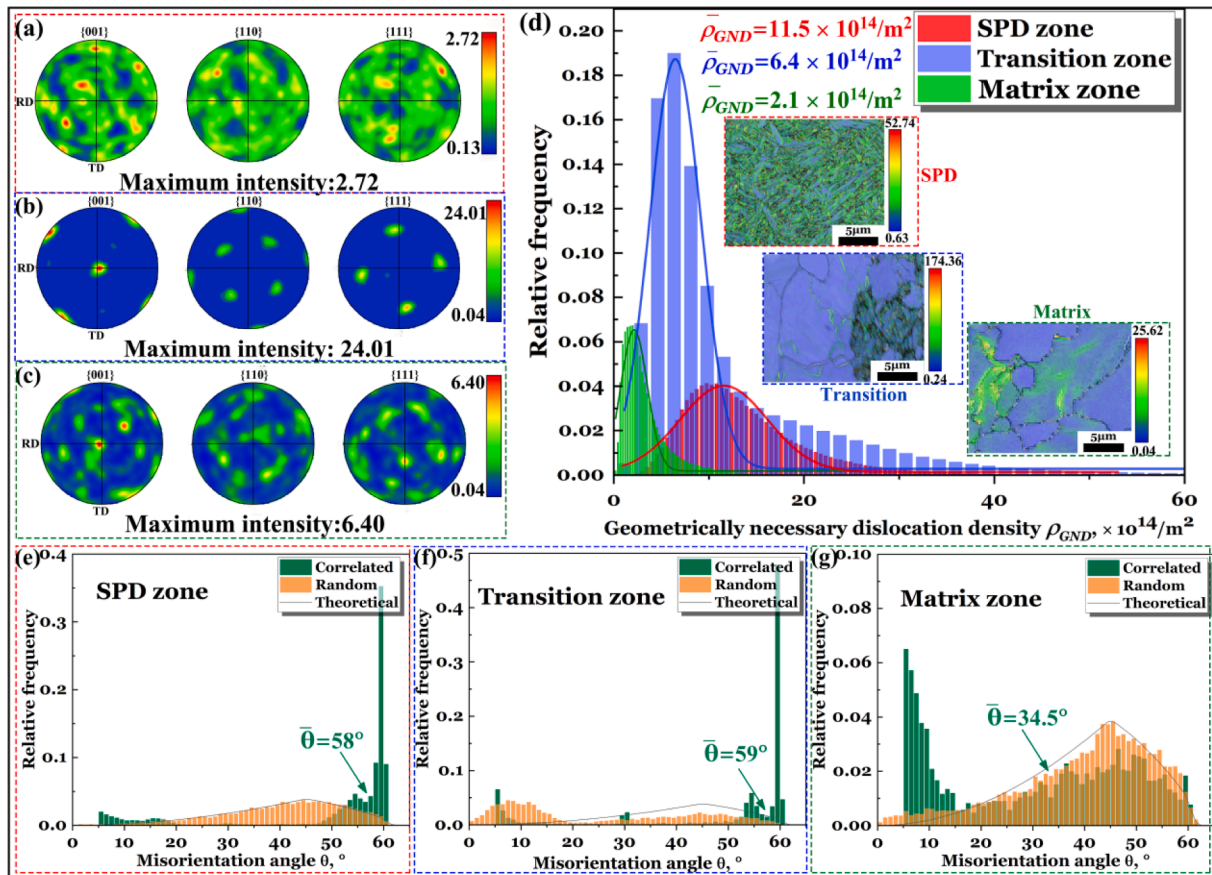
Fig. 11. Pole figures (PFs) of a specimen ($\sigma_{max} = 220$ MPa and $N_f = 1.01 \times 10^5$ cycles): (a) SPD zone, (b) transition zone and (c) matrix material; (d) data statistics of geometrically necessary dislocation density in three zones, where insets denoting respective GND map; disorientation angle distributions: (e) SPD zone, (f) transition zone and (g) matrix material.

in the vicinity of the inclusion. The inclusion surface in fractograph is nearly perpendicular to the loading direction, indicating that normal stress dominates crack initiation.

Fig. 8a is a fractograph (50 ms pause) containing two fish-eyes, and a facet with a distinct inclined angle exists within each fish-eye separately (Fig. 8b, c). EDS examinations shown in Fig. 8d, e give the chemical composition of the facet. The roughness range of fish-eye is above 200 μm, and the height range of facet reaches up to 29 μm (Fig. 8f), which distinguishes it from the case of inclusion. In addition, the specific inclined angle of facet (approximately 26° for both facets) was calculated by measuring the horizontal and height variation (Fig. 8g). By comparing profiles of crack initiation between rim (Fig. 7f) and WP (Fig. 8g), it can be seen that inclusion is more rough while facet is smooth and with inclined angle. It could be deduced that the rough inclusion surface attributes to normal stress (cyclic compressing) while smooth facet is an obvious result of shear stress.

3.4. Microstructure evolution

It is shown in Fig. 9 that the microstructure evolution of a rim specimen under fatigue loading with 50 ms pause as a function of the depth along longitudinal section from fracture surface. Here the longitudinal section can be divided into three distinct zones: severe plastic deformation (SPD) zone (≤1.0 mm below fracture surface), transition zone (1.0 mm ~ 1.5 mm below fracture surface) and matrix material (≥1.5 mm below fracture surface) as shown in a. The SEM observations show the microstructure evolution from (i) entire lamellar pearlite and ferrite (Fig. 9h) in matrix material, to (ii) newly-emerged martensite and isolated pearlite (Fig. 9e) in the transition zone, and eventually to (iii)

complete martensite-ferrite (Fig. 9b) in the SPD zone. Moreover, EBSD results give the changes of grain sizes (Fig. 10a) and their orientations by inverse pole figures (IPFs) with colors (Fig. 9c, f, i). Grain boundary plots (Fig. 9d, g, j) reveal the grain boundary angle and grain size with green curves representing low-angle grain boundaries (LAGBs) of 2° ~ 15° and black curves representing high-angle grain boundaries (HAGBs) of 15° ~ 65°. The microstructure variation along the depth from surface provides a hint to demonstrate the process of plastic deformation and defect accumulation in the specimens under loading with 50 ms pause.

In detail, the microstructure of matrix material is common lamellar pearlite with ferrite that was randomly distributed as shown in Fig. 9h and i, with the average equivalent grain size of 20.45 μm (Fig. 10a). In the transition zone, pearlitic colonies were compressed by normal stress and even some were severely fragmented (Fig. 9f), thus resulting in significantly reducing the grain size to 3.59 μm (sub-grains). In the SPD zone, acicular martensite was observed (Fig. 9b, c), indicating that phase transformation occurred due to self-heating induced in the fatigue loading with 50 ms pause. Furthermore, the coarse grains were continuously refined to ultra-fine grains with an average equivalent grain diameter of 1.89 μm. To further confirm the existence of martensite, micro-hardness was measured along longitudinal section. The results (Fig. 10b) show that SPD and transition zone possessed a substantially larger micro-hardness (824 ± 37 HV$_{0.5}$, 744 ± 67 HV$_{0.5}$, respectively) than that of matrix material (269 ± 28 HV$_{0.5}$).

In addition, grain boundary plots (Fig. 9d, g, j) present the obvious difference in the fraction of high-angle grain boundaries (HAGBs), demonstrating an increasing trend from matrix material (50%) to SPD zone (72.5%). This microstructure variation suggests that materials underwent dynamic recrystallization under fatigue loading with 50 ms
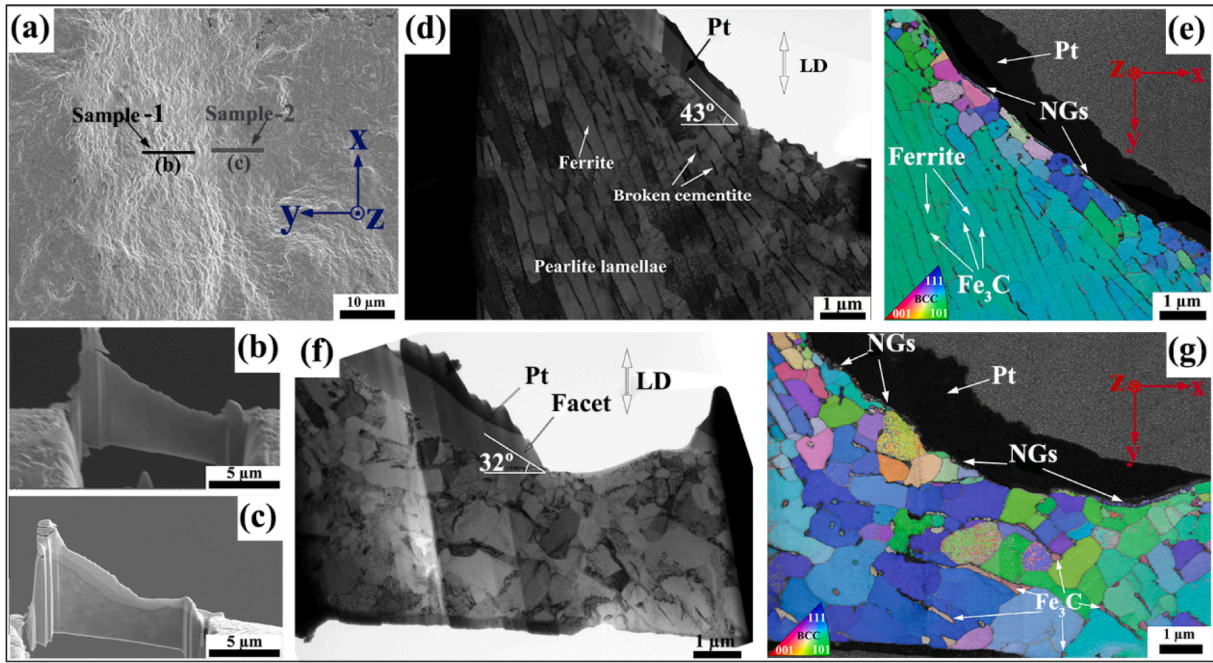
Fig. 12. (a) SEM image of a typical facet in Fig. 8b (web plate: $\sigma_{max} = 160$ MPa and $N_f = 1.66 \times 10^7$ cycles), (b) overall view of Sample-1 and (c) Sample-2; (d) TEM image of Sample-1 and (f) Sample-2; (e) TKD image of Sample-1 and (g) Sample-2.

pause, which is referred to as discontinuous dynamic recrystallization (dDRX) [45]. Discontinuous dynamic recrystallization is the process of new grain nucleation and growth, which usually takes place at high temperature ($450 \sim 650$ °C) [46]. Fig. 11a, b, c shows the pole figures (PFs) of three zones, where the intensity marked by colors represents the degree of preferential orientation of grains. The maximum intensity of transition zone is 24.01, which is markedly larger than that of matrix material (6.40) and SPD zone (2.72). The reason why the largest intensity occurred in the transition zone is the sliding of grains in the preferred direction, and the decrease of intensity in SPD zone can attribute to dDRX process. More specifically, dDRX has orientation randomizing effects [47], meaning that the process enables grains to rotate out of preceding preferred orientation during dDRX, and therefore weakens the formation of textures.

Moreover, the results of geometrically necessary dislocation densities (ρ_{GND}) for three zones are depicted in Fig. 11d, where insets denote their GND maps. The three zones from matrix material to SPD zone witnessed an increase in the values of ρ_{GND}, with 2.1 for matrix material, 6.4 for transition zone and 11.5 for SPD zone (units: $\times 10^{14}/m^2$), respectively. According to Ref. [45], dDRX has two distinct steps, which needs high level of dislocation density for the nucleation of new grains and migration of HABs, whereas ρ_{GND} decreases with large deformation
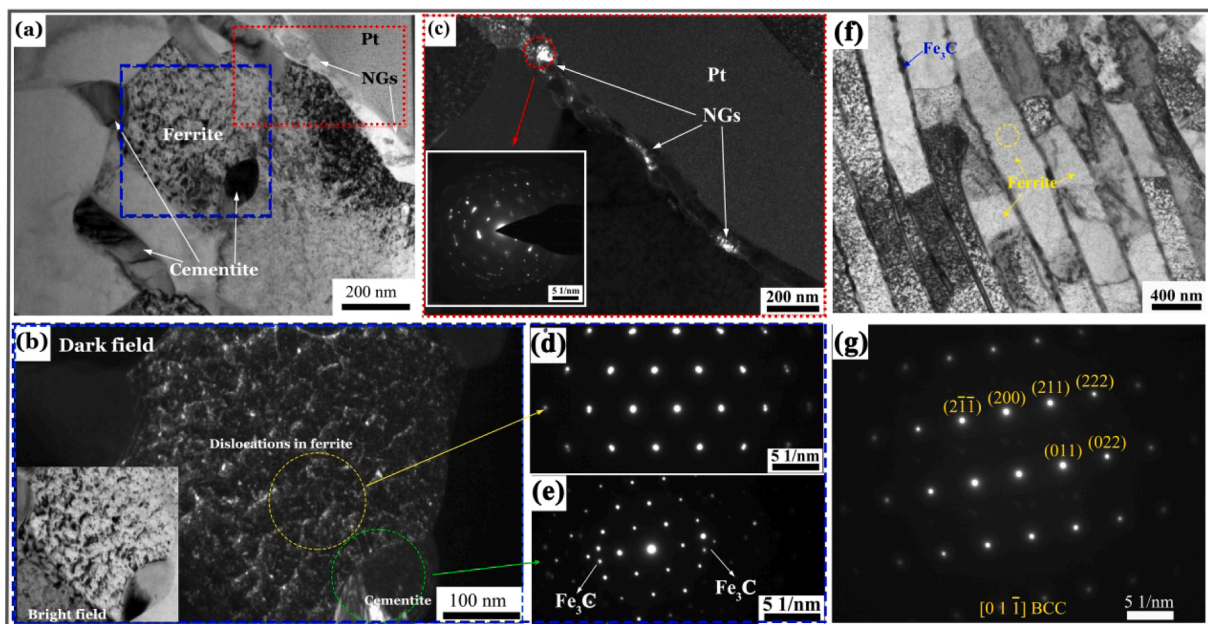

Fig. 13. (a) TEM image (web plate: $\sigma_{max} = 160$ MPa and $N_f = 1.66 \times 10^7$ cycles) in the vicinity of facet surface, the blue and red dotted squares denoting sites for dark field image of (b) and (c); (d) and (e) being selected area diffraction patterns of sites shown in (b); TEM image (f) and SAD patterns (g) of pearlitic lamellae.
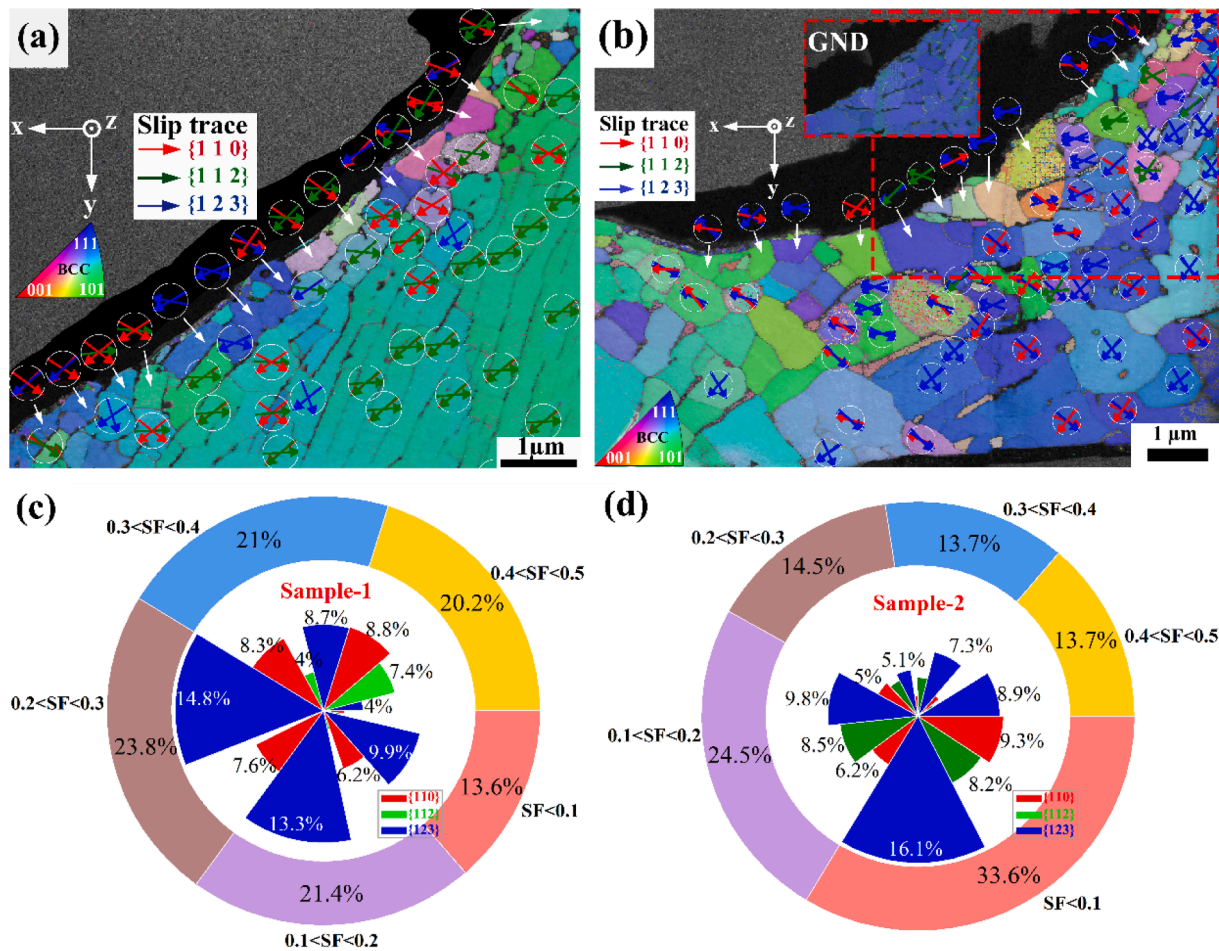
Fig. 14. (a) Slip traces with three largest SFs of grains beneath the facet including sample-1 and (b) sample-2; (c) statistical distribution of SFs for sample-1 and (d) sample-2, the inner pie charts denoting proportions of {110}, {112}, {123} slip plane families for each SF range.

induced by continuous dynamic recrystallization (cDRX) [46]. Therefore, the occurrence of dDRX was confirmed in the SPD zone during fatigue test with 50 ms pause. Fig. 11e, f, g show the distributions of grain boundary disorientation in three zones. "Correlated" means the calculation with neighboring data points and "Random" means the calculation randomly choosing pairs of data points from anywhere in the dataset, respectively. The average "correlated" disorientation angle in SPD and transition zones (58°) is significantly larger than that in matrix material (34.5°), demonstrating again that grains with LAGBs were transformed to fine grains with HAGBs.

3.5. Crack initiation and facet formation

A typical facet (Fig. 12a) of WP in the VHCF regime was chosen for FIB sampling, where Sample-1 and Sample-2 (Fig. 12b, c) were cut for the comparison of microstructures between facet and matrix. Fig. 12d, e exhibit TEM and TKD images of Sample-1, and Fig. 12f, g belong to Sample-2. By contrast, pearlitic lamellae approximately parallel to facet surface dominate the microstructure beneath the facet in comparison with Sample-2, indicating that the matrix with a specific orientation is in relation with facet formation. As shown in Fig. 12d, broken cementite can be found due to its brittleness. Meanwhile, the pearlitic lamellae possess similar orientation (Fig. 12e). By the comparison of TKD images between facet (Fig. 12e) and matrix (Fig. 12g), it is seen that pearlitic lamellae with similar orientation prevailed beneath facet while randomly oriented ferrite grains existed in matrix.

The observations of microstructural features for ferrite and cementite in facet and matrix are shown in Fig. 13. Fig. 13a is a TEM

image showing ferrite and cementite domains, where two local regions (colored by red and blue) were chosen for the detailed examination of its characteristics with dark field images, as shown in Fig. 13b and c. It is clearly seen that a large amount of dislocations prevailed in ferrite while no dislocations were observed in the cementite domain nearby (Fig. 13b). As shown in Fig. 13c, nanograins exist along the facet surface, where the inset diffraction pattern presents polycrystalline features within the selected area, which can be explained by the numerous cyclic pressing process [48] between crack surfaces. Furthermore, selected area diffraction patterns of two phases confirmed that body-centered cubic (BCC) structure for ferrite (Fig. 13d) and additional spots for Fe_3C (Fig. 13e). Moreover, the TEM image of Fig. 13f shows the lamellar feature of pearlite, suggesting that some dislocations in ferrite and the related selected area diffraction of Fig. 13g shows single crystal lattice.

For the further investigation of facet formation mechanism, the Schmid Factors (SFs) of 48 slip systems for each grain beneath the facet were calculated by Python programming. Euler angles of each grain were obtained by TKD, which were used to construct the rotation matrix between acquisition coordinate system and sample-based coordinate system. For BCC metal, 48 slip systems comprise {110}, {112} and {123} slip plane families with ⟨111⟩ slip directions. In order to calibrate the applied tension direction, we ensure the bottom border of thin foil is perpendicular to applied tension direction, and the side border is parallel to applied tension direction when sampling with FIB. Therefore we make sure that (0, −1, 0) is the tension direction according to TKD coordinate system shown in Fig. 14 a and b. According to Ref. [49], critical resolved shear stress (CRSS) of three slip plane families was confirmed comparable through micropillar compression tests. From that point, SF
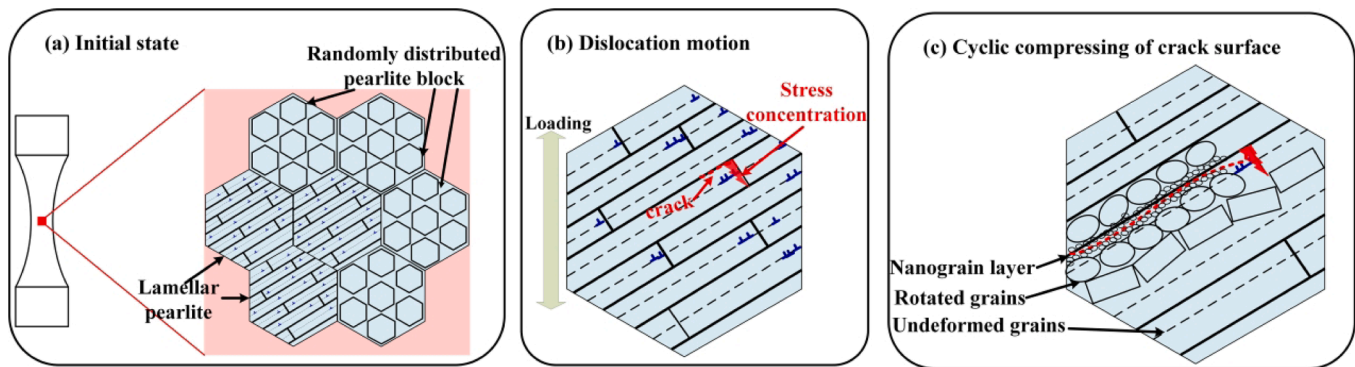
Fig. 15. Proposed mechanism of crack initiation and facet formation: (a) original microstructure before loading including randomly distributed pearlite block and pearlitic lamellae; (b) dislocation movement in ferrite and crack initiation at stress concentration site; (c) crack initiation along ferrite-cementite interface accompanied by grain refinement and rotation.

is regarded as the dominant cause for slip system activation. As shown in Fig. 14 a and b, three colorful arrows within a circle represent slip traces for each grain with three largest SFs. In this paper, the slip trace was defined as an intersecting line between slip plane (3 dimensional) and x-y plane (TKD image plane). Moreover, slip trace direction was determined by slip direction. In other words, the dot product between slip trace vector and slip direction vector is guaranteed to be positive. By contrast, {110} and {112} slip plane families dominated easy-activated slip systems for sample-1 (facet), whereas {123} occupied the majority of slip systems for sample-2 (matrix). According to Refs. [50–52], it became common practice to assume {110}⟨111⟩ and {112}⟨111⟩ slip systems at ambient temperature only, and slip traces on {123} is just evident in ferrite when reach higher temperature (compared with the critical transition temperature). Based on this view, we can deduce that slip on {110} {112} plane families promotes facet formation compared to matrix where slip on {123} plane families is hard to be activated.

On the other hand, cementite cannot be ignored because of its resistance to slip deformation when dislocations in ferrite move to the ferrite-cementite interface. Therefore, ferrite-cementite lamellae alignment is crucial in the determination of dislocation motion flexibility. According to Ref. [53], dislocations move freely in ferrite without encountering the ferrite-cementite interface only when the pearlitic lamellae are aligned at approximately 45° relative to the direction of applied tension. This can be confirmed by the calculated slip traces with the largest SF shown in Fig. 14a, b, where slip traces nearly show a 45° angle relative to the applied tension. Through the comparison of pearlitic alignment between facet (Fig. 12d) and matrix (Fig. 12f), it is concluded that pearlitic alignment at an angle of 45° promotes dislocations motion without obstacles, aggravating the inhomogeneous deformation between ferrite and cementite, which can be verified by the geometrically necessary dislocation densities plot (inset of Fig. 14b). Overall, the fatigue crack prefers to initiate from lamellar pearlite rather than randomly distributed pearlite block (Fig. 15a), as a result of stress concentration which occurs in the ferrite-cementite interface (Fig. 15b). Then crack initiates from this site and propagates along the interface. The nanograin layer is a result of numerous cyclic compressing after crack formation (Fig. 15c). This mechanism can explain why pearlitic lamellae are nearly aligned parallel to facet surface.

4. Conclusions

In this study, ultrasonic fatigue tests for both rim and web plate (WP) specimens under loading with 50 ms and 300 ms pause were conducted. The distinct microstructure evolution is obtained only in the specimens with acute self-heating under the condition of loading with 50 ms pause. The effects of fatigue loading intermittence on microstructure evolution and the mechanism of VHCF crack initiation were investigated. The main conclusions are as follows:

(1) Rim specimens possessed a higher fatigue strength than WP, which is attributed to a higher proportion of ferrite (soft phase) and larger pearlitic interlamellar spacing in WP. The difference of fatigue strength is a result of different cooling rates during water spray quenching for wheel tread.

(2) Fatigue cracks of rim specimens were prone to initiating from CaO·Al$_2$O$_3$ inclusion cluster (89.5%). In contrast, those of WP specimens preferred to initiate from matrix (82.1%), suggesting that matrix of WP is more detrimental than inclusion despite that the latter with relatively larger inclusion size.

(3) Self-heating induced in the fatigue loading with 50 ms pause cannot be neglected, since it triggered the microstructure evolution including grain refinement caused by discontinuous dynamic recrystallization (dDRX), and even led to martensitic transformation.

(4) Dislocation slip primarily on {110}, {112} plane families in ferrite enhanced inhomogeneous deformation, resulting in stress concentration in the ferrite-cementite interface. This promoted crack initiation and propagation along the interface, and ultimately facet nearly parallel to the interface was formed.

Declaration of Competing Interest

The authors declare that they have no known competing financial interests or personal relationships that could have appeared to influence the work reported in this paper.

Acknowledgements

References

[1] Zhu Y, Wang W, Lewis R, Yan W, Lewis SR, Ding H. A Review on Wear Between Railway Wheels and Rails Under Environmental Conditions. J Tribol 2019;141 (12):120801.

[2] Hu Y, Zhou L, Ding HH, Lewis R, Liu QY, Guo J, et al. Microstructure evolution of railway pearlitic wheel steels under rolling-sliding contact loading. Tribol Int 2021; 154:106685.

[3] Sakai T. Review and Prospects for Current Studies on Very High Cycle Fatigue of Metallic Materials for Machine Structural Use. Journal of Solid Mechanics and Materials Engineering 2009;3(3):425–39.

[4] Schuller R, Fitzka M, Irrasch D, Tran D, Pennings B, Mayer H. VHCF properties of nitrided 18Ni maraging steel thin sheets with different Co and Ti content. Fatigue Fract Eng Mater Struct 2015;38(5):518–27.

[5] Gao G, Liu R, Wang K, Gui X, Misra RDK, Bai B. Role of retained austenite with different morphologies on sub-surface fatigue crack initiation in advanced bainitic steels. Scr Mater 2020;184:12–8.

[6] Gao G, Wang K, Su H, Gui X, Li Z, Misra RDK, et al. The potential of mechanical twinning in ultrafine retained austenite to enhance high cycle fatigue property of advanced bainitic steels. Int J Fatigue 2020;139:105804.

[7] Zhao P, Gao G, Misra RDK, Bai B. Effect of microstructure on the very high cycle fatigue behavior of a bainite/martensite multiphase steel. Mater Sci Eng, A 2015; 630:1–7.

[8] Li G, Hong Z, Yan Q. The influence of microstructure on the rolling contact fatigue of steel for high-speed-train wheel. Wear 2015;342–343:349–55.

[9] Lee KM, Polycarpou AA. Wear of conventional pearlitic and improved bainitic rail steels. Wear 2005;259(1):391–9.

[10] Molyneux-Berry P, Davis C, Bevan A. The influence of wheel/rail contact conditions on the microstructure and hardness of railway wheels. ScientificWorldJournal 2014;2014:209752.

[11] Wang QY, Berard JY, Dubarre A, Baudry G, Rathery S, Bathias C. Gigacycle fatigue of ferrous alloys. Fatigue Fract Eng Mater Struct 1999;22(8):667–72.

[12] Furuya Y, Matsuoka S, Abe T, Yamaguchi K. Gigacycle fatigue properties for high-strength low-alloy steel at 100 Hz, 600 Hz, and 20 kHz. Scr Mater 2002;46(2): 157–62.

[13] Marines I, Dominguez G, Baudry G, Vittori JF, Rathery S, Doucet JP, et al. Ultrasonic fatigue tests on bearing steel AISI-SAE 52100 at frequency of 20 and 30 kHz. Int J Fatigue 2003;25(9–11):1037–46.

[14] Sun C, Song Q, Hu Y, Wei Y. Effects of intermittent loading on fatigue life of a high strength steel in very high cycle fatigue regime. Int J Fatigue 2018;117:9–12.

[15] Masoumi M, Ariza EA, Sinatora A, Goldenstein H. Role of crystallographic orientation and grain boundaries in fatigue crack propagation in used pearlitic rail steel. Mater Sci Eng, A 2018;722:147–55.

[16] Lojkowski W, Djahanbakhsh M, Bürkle G, Gierlotka S, Zielinski W, Fecht HJ. Nanostructure formation on the surface of railway tracks. Mater Sci Eng, A 2001; 303(1):197–208.

[17] T. Gladman, I.D. McIvor, F.B. Pickering, Some aspects of the structure–property relationships in high-carbon ferrite–pearlite steels, J Iron Steel Inst (London) 210 (part 12) (1972) 916-930.

[18] Hui W, Zhang Y, Shao C, Chen S, Zhao X, Dong H. Effect of Cooling Rate and Vanadium Content on the Microstructure and Hardness of Medium Carbon Forging Steel. J Mater Sci Technol 2016;32(6):545–51.

[19] Feng H, Cai L, Wang L, Zhang X, Fang F. Microstructure and strength in ultrastrong cold-drawn medium carbon steel. J Mater Sci Technol 2022;97:89–100.

[20] Cong T, Han JM, Hong YS, Domblesky JP, Liu XL. Shattered rim and shelling of high-speed railway wheels in the very-high-cycle fatigue regime under rolling contact loading. Eng Fail Anal 2019;97:556–67.

[21] Eyre TS, Baxter A. The formation of white layers at rubbing surfaces. Tribology 1972;5(6):256–61.

[22] Ivanisenko Y, Lojkowski W, Valiev RZ, Fecht HJ. The mechanism of formation of nanostructure and dissolution of cementite in a pearlitic steel during high pressure torsion. Acta Mater 2003;51(18):5555–70.

[23] Liu CP, Zhang GZ, Liu PT, Chen CH, Ren RM. An electron backscatter diffraction investigation on microstructural evolution of pearlite wheel steel near rolling contact fatigue crack tip. Fatigue Fract Eng Mater Struct 2021;44(8):2244–56.

[24] Shiozawa K, Lu L, Ishihara S. S-N curve characteristics and subsurface crack initiation behaviour in ultra-long life fatigue of a high carbon-chromium bearing steel. Fatigue Fract Eng Mater Struct 2001;24(12):781–90.

[25] Hong Y, Lei Z, Sun C, Zhao A. Propensities of crack interior initiation and early growth for very-high-cycle fatigue of high strength steels. Int J Fatigue 2014;58: 144–51.

[26] Jiang Y, Zhang B, Wang D, Zhou Y, Wang J, Han E-H, et al. Hydrogen-assisted fracture features of a high strength ferrite-pearlite steel. J Mater Sci Technol 2019; 35(6):1081–7.

[27] Chai G. The formation of subsurface non-defect fatigue crack origins. Int J Fatigue 2006;28(11):1533–9.

[28] Zhang J, Li S, Yang Z, Li G, Hui W, Weng Y. Influence of inclusion size on fatigue behavior of high strength steels in the gigacycle fatigue regime. Int J Fatigue 2007; 29(4):765–71.

[29] Zhou C, Wang M, Hui W, Dong H, Wang L, Wu R. Rotating bending fatigue properties of two case hardening steels after nitriding treatment. Mater Des 2013; 46:539–45.

[30] Grigorescu AC, Hilgendorff PM, Zimmermann M, Fritzen CP, Christ HJ. Cyclic deformation behavior of austenitic Cr–Ni-steels in the VHCF regime: Part I - Experimental study. Int J Fatigue 2016;93:250–60.

[31] Hilgendorff P-M, Grigorescu AC, Zimmermann M, Fritzen C-P, Christ H-J. Cyclic deformation behavior of austenitic Cr–Ni-steels in the VHCF regime: Part II – Microstructure-sensitive simulation. Int J Fatigue 2016;93:261–71.

[32] Zimmermann M. Diversity of damage evolution during cyclic loading at very high numbers of cycles. Int Mater Rev 2013;57(2):73–91.

[33] Sander M, Müller T, Lebahn J. Influence of mean stress and variable amplitude loading on the fatigue behaviour of a high-strength steel in VHCF regime. Int J Fatigue 2014;62:10–20.

[34] Huang Z, Wagner D, Bathias C, Paris PC. Subsurface crack initiation and propagation mechanisms in gigacycle fatigue. Acta Mater 2010;58(18):6046–54.

[35] Li W, Deng H, Sun Z, Zhang Z, Lu L, Sakai T. Subsurface inclusion-induced crack nucleation and growth behaviors of high strength steels under very high cycle fatigue: Characterization and microstructure-based modeling. Mater Sci Eng, A 2015;641:10–20.

[36] Gao G, Xu Q, Guo H, Gui X, Zhang B, Bai B. Effect of inclusion and microstructure on the very high cycle fatigue behaviors of high strength bainite/martensite multiphase steels. Mater Sci Eng, A 2019;739:404–14.

[37] Pan X, Xu S, Qian G, Nikitin A, Shanyavskiy A, Palin-Luc T, et al. The mechanism of internal fatigue-crack initiation and early growth in a titanium alloy with lamellar and equiaxed microstructure. Mater Sci Eng, A 2020;798:140110.

[38] Pan X, Su H, Sun C, Hong Y. The behavior of crack initiation and early growth in high-cycle and very-high-cycle fatigue regimes for a titanium alloy. Int J Fatigue 2018;115:67–78.

[39] Hu X, Van Houtte P, Liebeherr M, Walentek A, Seefeldt M, Vandekinderen H. Modeling work hardening of pearlitic steels by phenomenological and Taylor-type micromechanical models. Acta Mater 2006;54(4):1029–40.

[40] Mayer H. Recent developments in ultrasonic fatigue. Fatigue Fract Eng Mater Struct 2016;39(1):3–29.

[41] Li W, Sakai T, Li Q, Lu L, Wang P. Reliability evaluation on very high cycle fatigue property of GCr15 bearing steel. Int J Fatigue 2010;32(7):1096–107. https://doi.org/10.1016/j.ijfatigue.2009.12.008.

[42] Appendix C - Probability sheets of statistics of extremes, in: Y. Murakami (Ed.), Metal Fatigue (Second Edition), Academic Press2019, pp. 717-718.

[43] Yu Y, Gu JL, Xu L, Shou FL, Bai BZ, Liu YB. Very high cycle fatigue behaviors of Mn–Si–Cr series Bainite/Martensite dual phase steels. Mater Des 2010;31(6): 3067–72.

[44] Peng W, Zhang Y, Qiu B, Xue H. A Brief Review of the Application and Problems in Ultrasonic Fatigue Testing. AASRI Procedia 2012;2:127–33.

[45] Sakai T, Belyakov A, Kaibyshev R, Miura H, Jonas JJ. Dynamic and post-dynamic recrystallization under hot, cold and severe plastic deformation conditions. Prog Mater Sci 2014;60:130–207.

[46] Hu Y, Zhou L, Ding HH, Lewis R, Liu QY, Guo J, et al. Microstructure evolution of railway pearlitic wheel steels under rolling-sliding contact loading. Tribol Int 2021; 154:106685.

[47] Montheillet F, Cohen M, Jonas JJ. Axial stresses and texture development during the torsion testing of Al. Cu and α-Fe, Acta Metallurgica 1984;32(11):2077–89.

[48] Hong Y, Liu X, Lei Z, Sun C. The formation mechanism of characteristic region at crack initiation for very-high-cycle fatigue of high-strength steels. Int J Fatigue 2016;89:108–18.

[49] Tian C, Ponge D, Christiansen L, Kirchlechner C. On the mechanical heterogeneity in dual phase steel grades: Activation of slip systems and deformation of martensite in DP800. Acta Mater 2020;183:274–84.

[50] Opinsky AJ, Smoluchowski R. The Crystallographic Aspect of Slip in Body-Centered Cubic Single Crystals. II. Interpretation of Experiments. J Appl Phys 1951; 22(12):1488–92.

[51] Nine HD. Slip planes and asymmetric slip in fatigue of iron single crystals. Phil Mag 2006;26(6):1409–18.

[52] Tian C, Dehm G, Kirchlechner C. Influence of strain rate on the activation of 110}, {112}, {123 slip in ferrite of DP800. Materialia 2021;15:100983.

[53] Teshima T, Kosaka M, Ushioda K, Koga N, Nakada N. Local cementite cracking induced by heterogeneous plastic deformation in lamellar pearlite. Mater Sci Eng, A 2017;679:223–9.